



Article

A First-Time Addition of Selenium to a Mg-Based Metal Matrix Composite for Biomedical Purposes

Ahluwalia Pahaul, Michael Johanes and Manoj Gupta *

Department of Mechanical Engineering, National University of Singapore, 9 Engineering, Drive 1, Singapore 117575, Singapore

* Correspondence: mpegm@nus.edu.sg

Abstract: A magnesium-based metal matrix composite, Mg-5Se-2Zn-2SiO₂, was synthesized using the Disintegrated Melt Deposition (DMD) method followed by hot extrusion. Elemental analysis revealed that the material experienced selenium loss which was attributed to the evaporation of selenium at high temperatures. Superior damping characteristics were exhibited while retaining similar Young's modulus, and significant grain refinement also resulted in decisively superior mechanical properties such as hardness (32% increase), fracture strain (39% increase), as well as yield and ultimate compressive strength (157% and 54% increase, respectively). These were a consequence of SiO₂ addition as well as presence of Mg₂Si (and MgSe) intermetallic phases which were detected by X-ray characterization. Furthermore, while the material had lower corrosion resistance than pure magnesium, it retained acceptable corrosion resistance as well as structural integrity after the full immersion duration of 28 days. Overall, the material exhibits promising potential for applications in the biomedical field, especially in development of smaller and lighter implants where mechanical properties are paramount, with key lessons learned for the synthesis of Mg-materials containing selenium for the future.

Keywords: magnesium; metal matrix composites; biomedical; disintegrated melt deposition; lightweight materials; mechanical properties



Citation: Pahaul, A.; Johanes, M.; Gupta, M. A First-Time Addition of Selenium to a Mg-Based Metal Matrix Composite for Biomedical Purposes. *J. Compos. Sci.* **2024**, *8*, 81. <https://doi.org/10.3390/jcs8030081>

Academic Editor: Francesco Tornabene

Received: 5 January 2024

Revised: 7 February 2024

Accepted: 19 February 2024

Published: 22 February 2024



Copyright: © 2024 by the authors. Licensee MDPI, Basel, Switzerland. This article is an open access article distributed under the terms and conditions of the Creative Commons Attribution (CC BY) license (<https://creativecommons.org/licenses/by/4.0/>).

1. Introduction

Biomaterials are used in numerous fields such as dentistry, orthopaedics, drug delivery systems, cardiovascular devices as well as skin tissue engineering [1]. Conventional materials used in these fields include stainless steel, cobalt-based alloys, and titanium alloys. However, issues such as stress shielding and the release of toxic metal ions are drawbacks to these conventional materials [2]. Furthermore, these materials are not biodegradable, so further surgery to remove these implants is traditionally a norm.

As a result, over the last few years, bioresorbable materials such as magnesium (Mg) [3] have been gaining attention as it has a very high in vitro corrosion rate of 400 mm/year (as-cast condition) [4], with non-toxic by-products. This also eliminates the need for any secondary surgeries for implant removal. Additionally, magnesium is the lightest structural metal, being 50% lighter than titanium [5] per unit volume. Lastly, the mechanical properties of magnesium, such as high specific strength and low density, are comparable with that of human bone, which can resolve the issue of stress shielding [6]. All these characteristics showcase the suitability of magnesium for biomedical use, hence providing an impetus for studies on Mg-based materials tailored for biomedical applications.

Zinc, magnesium, selenium and silicon are essential/trace elements required by the human body for various bodily functions. Zhang et al. demonstrated that the addition of zinc to magnesium can reduce the corrosion rate and the resultant alloy has improved mechanical properties, all whilst exhibiting biocompatibility [7]. Additionally, selenium plays important roles in the human body, including the catalysis of enzymes in the human

body (as well as substances mimicking these catalysts) [8,9], prevention of various chronic diseases (with appropriate supplement doses) [10], and anti-cancer as well as antioxidative properties with regard to cells [11]. Furthermore, combining selenium and magnesium intake has shown promise as a therapeutic strategy in the protection of the liver against hyperlipidaemia, achieved partially via antioxidative effects in animal trials [12]. An improved mechanical response through the addition of SiO₂ to magnesium has also been demonstrated; a study by Wan et al. revealed that such addition of 45S5 bioglass to pure magnesium increased its compressive strength by 18% [13].

Metal matrix composites (MMCs) comprise a metallic base reinforced with a suitable reinforcement. Nanoparticles added in Mg-based metal matrix composites were observed to exhibit strengthening effects [14], with excellent mechanical properties such as high strength, high stiffness, and wear resistance whilst maintaining the fracture toughness [15]. The addition of nanoparticles to magnesium matrix composites can help attain a better balance between strength and plasticity [14]. Due to these enhancements in properties, magnesium MMCs could potentially be used in biomedical sectors as a substitute for traditional magnesium alloys and/or composites [16].

These considerations provide an impetus for an investigation on a Mg-based MMC for potential biomedical applications, namely that of Mg-5Se-2Zn-2SiO₂ (wt.%), to explore its properties. Accordingly, the objective of the present study was to gain an initial understanding of a nanocomposite system containing selenium. This is to be combined with the Disintegrated Melt Deposition (DMD) method, which has been used since the mid-1990s with a variety of Mg-materials, including multicomponent alloys and nanocomposites, to synthesize materials with good results [17,18]. To the authors' knowledge, this is the first study in which selenium, a trace and medicinal element (recommended dietary allowance of 55 µg for adults [19]), has been used as an alloying element in a nanocomposite system.

2. Experimental Procedure

2.1. Synthesis

The raw materials used in the synthesis of Mg-5Se-2Zn-2SiO₂ are outlined in Table 1.

Table 1. List of raw materials used in this study.

Material	Supplier	Purity
Magnesium Turnings	Acros Organics, Morris Plains, NJ, USA	>99.9%
Zinc Shots		99.99%
Selenium Powder	Alfa Aesar GmbH & Co KG, Haverhill, MA, USA	99.999%
SiO ₂ nanoparticles, 10–20 nm		99.5%

The ingot was synthesized using Disintegrated Melt Deposition (DMD) with a target superheat temperature of 750 °C, followed by stirring for 5 min at 500 rpm using a steel impeller, with argon as the inert gas during this process. This process resulted in an ingot of 40 mm diameter and Figure 1 shows a schematic of the DMD process.

This ingot was then machined to billets of 35.5 mm diameter and 45 mm length. These billets were then soaked at 200 °C for 60 min, followed by hot extrusion with a die temperature of 350 °C using a 8 mm diameter die.

2.2. Microstructural Characterization

The sample was polished and finished with 0.05 micron alumina suspension and thereafter it was observed using a Hitachi S-4300 Field Emission Scanning Electron Microscope (FESEM, Hitachi, Ltd., Tokyo, Japan) to characterize the microstructure. Energy-Dispersive Spectroscopy (EDS) was performed to gain insight into the distribution of constituent elements within the microstructure.

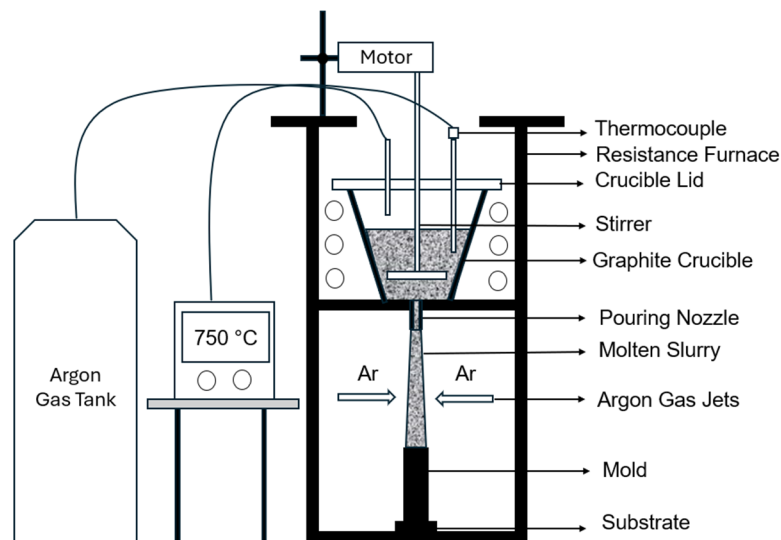


Figure 1. Schematic diagram of the DMD process.

For X-ray Diffraction (XRD) studies, the sample was ground flat for both the cross-sectional and longitudinal surfaces. Using the Shimadzu XRD-6000 Automatic Spectrometer (Shimadzu Corporation, Kyoto, Japan), these surfaces were then subjected to Cu K(α) X-rays with wavelengths of 1.5418 Å with a scanning speed of 2 degrees/minute and scanning range of 10° to 80° to obtain the diffraction peaks, which were compared against standard values found in the literature.

For grain size characterization, the polished samples were etched with a solution of 1 mL acetic acid and 49 mL H₂O for 2 s. Grain images were obtained using a JEOL JSM-6010PLUS/LV Scanning Electron Microscope (SEM, JEOL USA Inc., Peabody, MA, USA); thereafter, these images were analysed using the ImageJ software (version 1.54g, National Institutes of Health, Bethesda, MD, USA) to find the grain size.

2.3. Density and Porosity

The mass of 5 samples was measured in air and deionized (DI) water using a GH-252 electronic scale equipped with an AD-1653 Density Determination Kit (AND Company, Limited, Tokyo, Japan); thereafter, the Archimedes principle was used to find the experimental density.

Two freshly ground samples, each weighing approximately 2 mg, were dissolved by acid digestion: one in a solution of HNO₃ and HCl (ratio of 1:3), and the other in a solution of HNO₃, HCl, and HF (ratio of 1:3:1). The resulting acid–water matrices were then characterized for elemental composition using a Perkin Elmer Avio 500 Inductively Coupled Plasma-Optical Emission Spectrometer (ICP-OES, from PerkinElmer, Inc., Waltham, MA, USA) to obtain the weight fraction of individual elements in the material. The theoretical density was calculated using the rule of mixtures, based on the results obtained from the elemental analysis.

Experimental porosity was characterized by firstly obtaining pore images of the material, followed by image analysis with the ImageJ software (version 1.54g, National Institutes of Health, Bethesda, MD, USA) to obtain the pore area fraction and thus the corresponding experimental porosity of the MMC.

2.4. Damping Characterization

A sample of length 50 mm was subjected to impulse excitation. The resulting vibration was recorded by the RFDA Software version 8.1.2 (IMCE, Genk, Belgium), and thereafter analysed to find damping properties such as the attenuation coefficient, Young's modulus and damping capacity.

2.5. Mechanical Characterization

Using a Shimadzu HMV 02 automatic digital hardness tester (Shimadzu Corporation, Kyoto, Japan), a sample was subjected to a 245.2 mN force load with a dwell time of 15 s for a minimum of 15 readings, as per the ASTM E-384 standard to obtain microhardness values.

For compressive testing, samples were ground to a 4000 grit finish to obtain a sample with a length-to-diameter ratio of 1. These samples were then subjected to a quasi-static compressive load at a strain rate of 0.0083%/s until failure using the MTS E-44 compressive tester machine (MTS Systems, Eden Prairie, MN, USA) in accordance with ASTM E9-09 standard.

The fractured samples from compression test were observed using a JEOL JSM-6010PLUS/LV SEM (JEOL USA Inc., Peabody, MA, USA). This was performed to analyse the fracture surface.

2.6. Corrosion Testing

Two samples of approximately 2 mm length were ground to 4000 grit. These were then submerged in Phosphate Buffer Saline (PBS, Thermo Fisher Scientific Inc., Waltham, MA, USA) in a water bath, where a temperature of 37 °C was maintained. The sample was then immersed in 1.9 g of AgNO₃ and 20 g of CrO₃ in 100 mL of deionized water to remove corrosion products and rinsed with deionized water. Thereafter, it was dried and weighed to measure weight loss. This was performed in 24 h intervals, for up to 28 days or until sample failure/disintegration. Using the formula mentioned below and the weight reduction, corrosion rate can be calculated:

$$\text{Corrosionrate (mm/year)} = \frac{87.6 \times W}{\text{DAT}} \quad (1)$$

where W is weight loss in mg, D is the experimental density of the samples in g/cm³, A is the surface area of the samples in cm² and T is immersion duration in hours.

2.7. Thermal Characterization

A sample of approximately 2 mm × 2 mm × 2 mm was exposed to a temperature range of 30 °C to 1400 °C at 10 °C per min in purified air, with a flow rate of 50 mL per minute, using the Shimadzu DTG-60H Thermogravimetric Analyser (Shimadzu Corporation, Kyoto, Japan) to determine ignition temperature.

A sample of approximately 2 mm × 2 mm × 2 mm was exposed to a temperature range of 30 °C to 600 °C at a rate of 5 °C per minute in argon gas of 25 mL per minute flow rate, using the Shimadzu DSC-60 Digital Scanning Calorimeter (Shimadzu Corporation, Kyoto, Japan), to determine its thermal response.

A sample of 4 mm length and 8 mm diameter was exposed to temperature range of 50 °C to 400 °C at a rate of 5 °C per minute in argon gas of 0.1 L per minute flow rate, using the TMA PT1000 Thermo-mechanical analyser (Linseis Messgeraete GmbH, Selb, Germany), to determine the coefficient of thermal expansion (CTE).

3. Results

3.1. Synthesis

The material was cast, machined, and extruded successfully, shown in Figure 2. However, it was noted that red-coloured deposits were observed above the DMD setup, implying that selenium had evaporated during the DMD process. It was also noticed that after some time, red spots appeared on the surface of machined billets and (to a lesser extent) on ground samples, though these were not present on polished samples.

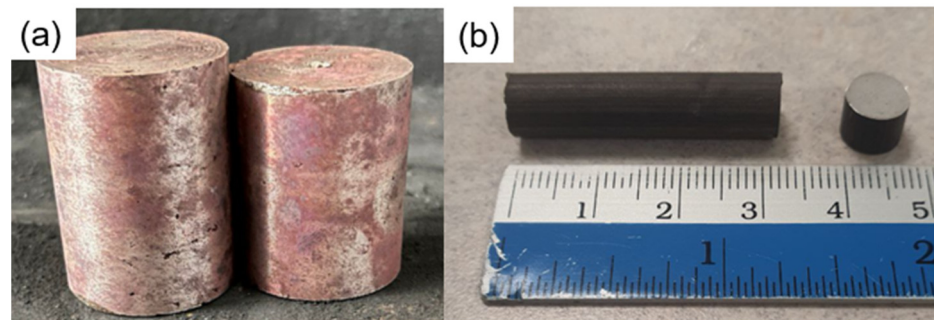


Figure 2. (a) Machined Mg-5Se-2Zn-2SiO₂ and (b) extruded Mg-5Se-2Zn-2SiO₂, showing part of the rod and a polished sample.

3.2. General Microstructure

Figures 3 and 4 as well as Table 2 show the microstructure and EDS results of selected areas within the microstructure, with pores also visible. While most of the material is composed of the Mg matrix (with dissolved Zn; spectrum 2), there are some bright regions exhibiting a Se and O content in conjunction with Mg (spectrum 1), as well as regions with a Mg, O, and Si content (spectrum 3).

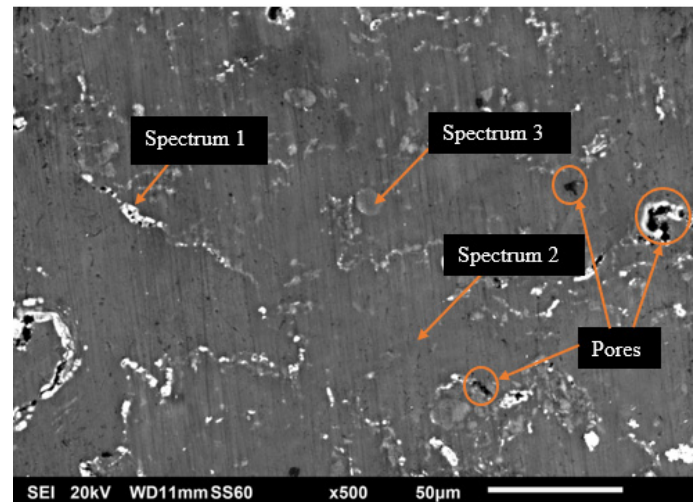


Figure 3. Scanning electron micrograph of Mg-5Se-2Zn-2SiO₂.

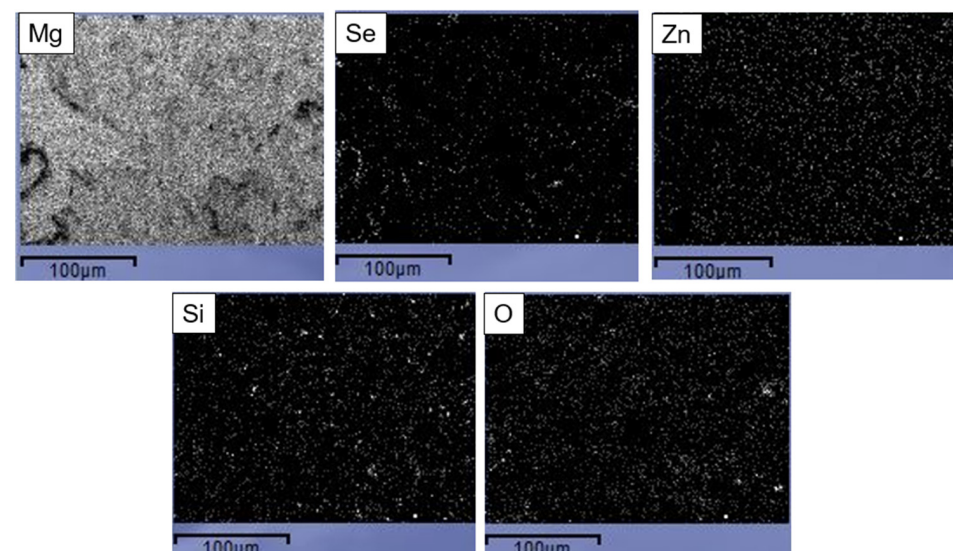


Figure 4. Mapping results of Mg-5Se-2Zn-2SiO₂.

Table 2. Atomic weight fractions of detected elements in Mg-5Se-2Zn-2SiO₂ at selected spectrum locations.

Spectrum	Detected Element (at %)				
	Mg	O	Se	Si	Zn
1	55.59	18.69	25.71	-	-
2	98.82	-	-	-	1.18
3	86.32	11.05	-	1.43	1.19

The XRD diffractogram of Mg-5Se-2Zn-2SiO₂ is plotted in Figure 5, with the following JCPDS card numbers referenced using the PDF-4+ (2023) database [20]: 00-004-0770 (Mg), 00-035-0773 (Mg₂Si), 00-004-0829 (MgO), 00-051-1389 (Se), and 01-073-6986 (MgSe).

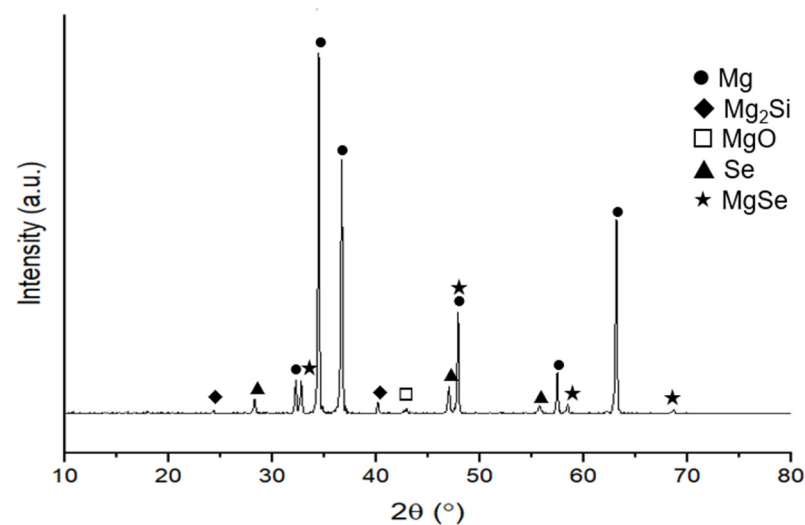


Figure 5. Diffractogram of Mg-5Se-2Zn-2SiO₂ on longitudinal surface.

Table 3 compares the average grain size for the Mg-5Se-2Zn-2SiO₂ matrix composite with pure magnesium. The average grain diameter of Mg-5Se-2Zn-2SiO₂ is a fifth of the grain diameter of pure magnesium.

Table 3. Grain properties of Mg-5Se-2Zn-2SiO₂ and pure magnesium as a reference.

Material	Average Grain Size (μm)
Pure Mg * [21]	25 ± 4
Mg-5Se-2Zn-2SiO ₂	5 ± 2 (↓80%)

* Material has been synthesized using a similar method (DMD followed by hot extrusion).

3.3. Density and Porosity

Table 4 shows the results of elemental analysis, containing the weight fractions of the individual alloying elements and reinforcements added, showing significant selenium loss.

Table 4. Elemental analysis test results for Mg-5Se-2Zn-2SiO₂ composite.

Detected Element/Compound (wt. %)			
Mg	Se	SiO ₂	Zn
95.94	0.66	1.26	2.14

The characterized experimental density and porosity are outlined in Table 5. The theoretical density was calculated using the rule of mixtures based on results from the elemental analysis. The experimental porosity was derived from the pore area fraction.

Table 5. Density and porosity results for Mg-5Se-2Zn-2SiO₂ with pure magnesium as a reference.

Material	Theoretical Density (g/cc)	Experimental Density (g/cc)	Porosity (%)
Pure Mg * [21]	1.738	1.727 ± 0.020	0.648
Mg-5Se-2Zn-2SiO ₂	1.782 (↑3%)	1.846 ± 0.011 (↑7%)	0.445 (↓31%)

* Material has been synthesized using similar method (DMD followed by hot extrusion).

The experimental density for the Mg-5Se-2Zn-2SiO₂ matrix composite was approximately 7% higher than pure magnesium whilst the experimental porosity was 31% lower than pure magnesium.

3.4. Damping Characterization

The results of the damping test conducted are outlined in Table 6 and Figure 6.

Table 6. Damping results Mg-5Se-2Zn-2SiO₂ with pure magnesium as a reference.

Material	Attenuation Coefficient	Damping Capacity	E-Modulus (GPa)
Pure Mg * [21]	5.709	-	44.00
Mg-5Se-2Zn-2SiO ₂	15.89 (↑178%)	0.000422	45.47 (↑3%)

* Material has been synthesized using similar method (DMD followed by hot extrusion).

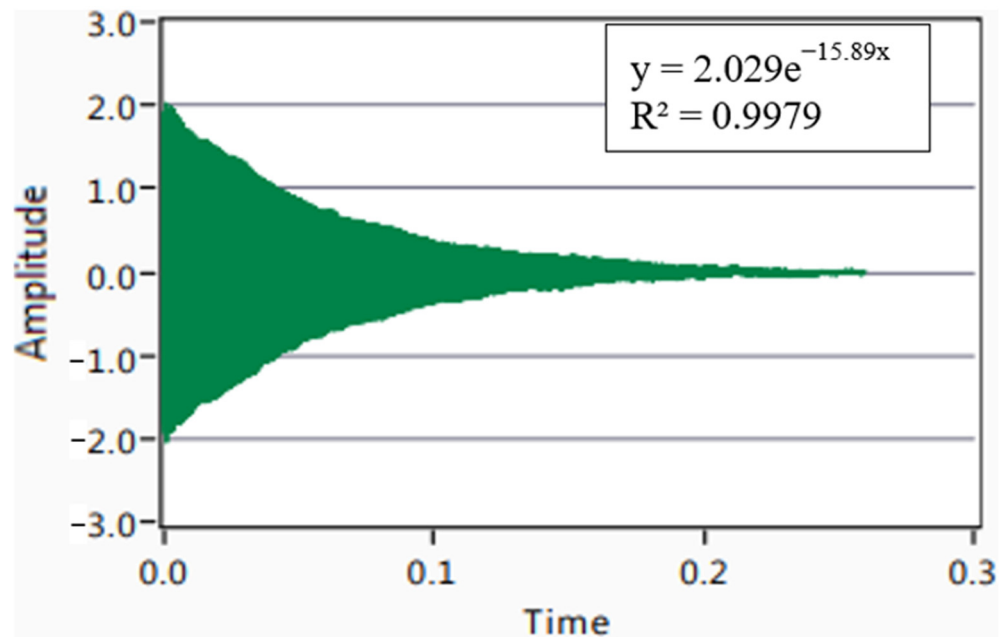


Figure 6. Damping profile of Mg-5Se-2Zn-2SiO₂ composite.

Comparing the properties of Mg-5Se-2Zn-2SiO₂ to the pure magnesium, it can be noticed that the attenuation coefficient of the metal matrix composite was approximately triple that of pure magnesium. Additionally, Young’s modulus of Mg-5Se-2Zn-2SiO₂ was similar to that of pure magnesium (3% higher).

3.5. Mechanical Characterization

The microhardness results are stated in Table 7, showing a significant improvement over pure Mg.

The Mg-5Se-2Zn-2SiO₂ showed an increase in Vickers’s hardness by 32% when compared to pure magnesium. The resulting compression properties are outlined in Table 8, while the stress–strain curves of pure Mg and Mg-5Se-2Zn-2SiO₂ are shown in Figure 7.

Table 7. Microhardness results for Mg-5Se-2Zn-2SiO₂ and pure magnesium as a reference.

Material	Average Hardness (Hv)
Pure Mg * [21]	66 ± 3
Mg-5Se-2Zn-2SiO ₂	87 ± 4 (↑32%)

* Material has been synthesized using similar method (DMD followed by hot extrusion).

Table 8. Compression properties for Mg-5Se-2Zn-2SiO₂ and pure magnesium as a reference.

Material	Mean 0.2% Yield Strength (MPa)	Mean Ultimate Compressive Strength (MPa)	Mean Fracture Strain (%)	Mean Energy Absorbed (MJ/m ³)
Pure Mg * [21]	70 ± 8	314 ± 14	23 ± 3	42 ± 4
Mg-5Se-2Zn-2SiO ₂	183 ± 3 (↑157%)	485 ± 15 (↑54%)	32 ± 1 (↑39%)	89 ± 9 (↑112%)

* Material has been synthesized using similar method (DMD followed by hot extrusion).

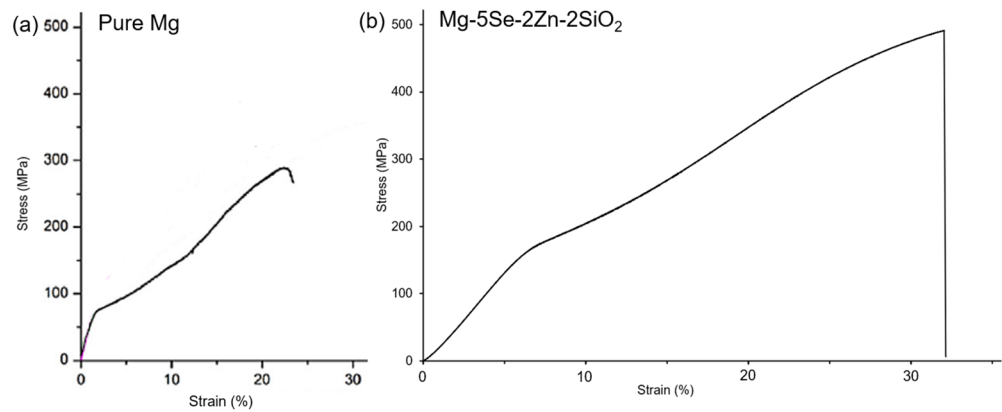


Figure 7. Compressive stress–strain curves of (a) Pure Mg [21] and (b) Mg-5Se-2Zn-2SiO₂ composite. Reprinted from Journal of Alloys and Compounds, Vol. 689, Tekumalla et al., Enhancing overall static/dynamic/damping/ignition response of magnesium through the addition of lower amounts (<2%) of yttrium, 350–358, Copyright (2016), with permission from Elsevier.

Mg-5Se-2Zn-2SiO₂ was found to have a higher 0.2% yield strength (157% higher), ultimate compressive strength (54% higher), mean fracture strength (39% higher) and energy absorbed (112% higher) when compared to pure magnesium. Figures 8 and 9 show the macroscopic fractured sample as well as the fracture surface of the magnesium matrix sample, respectively.



Figure 8. Photograph of compressively fractured Mg-5Se-2Zn-2SiO₂, showing the 45° angle of fracture.

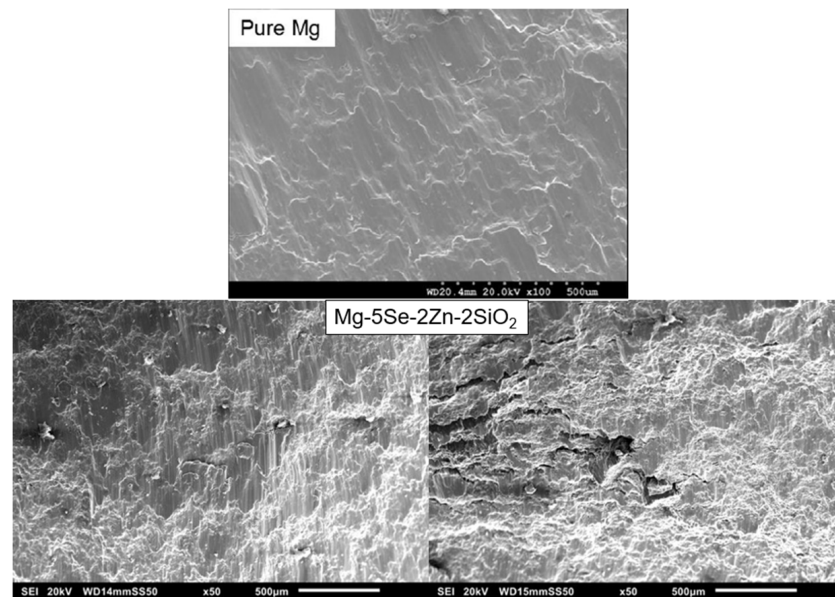


Figure 9. Fracture surfaces of (top) pure Mg [21] and (bottom) Mg-5Se-2Zn-2SiO₂, showing shear bands as well as cracks on the fracture surface of the latter. Reprinted from Journal of Alloys and Compounds, Vol. 689, Tekumalla et al., Enhancing overall static/dynamic/damping/ignition response of magnesium through the addition of lower amounts (<2%) of yttrium, 350–358, Copyright (2016), with permission from Elsevier.

The shear bands can be observed across the surface in the SEM images in Figure 9, though the Mg-5Se-2Zn-2SiO₂ material exhibited noticeably more cracks than pure Mg (which only exhibited shear bands). Some cracks were also present on the fracture surface. Additionally, the approximate angle of fracture was 45° from the axis of compression.

3.6. Corrosion Testing

Figure 10 shows the trend of average corrosion rate with time submerged for Mg-5Se-2Zn-2SiO₂ in PBS solution.

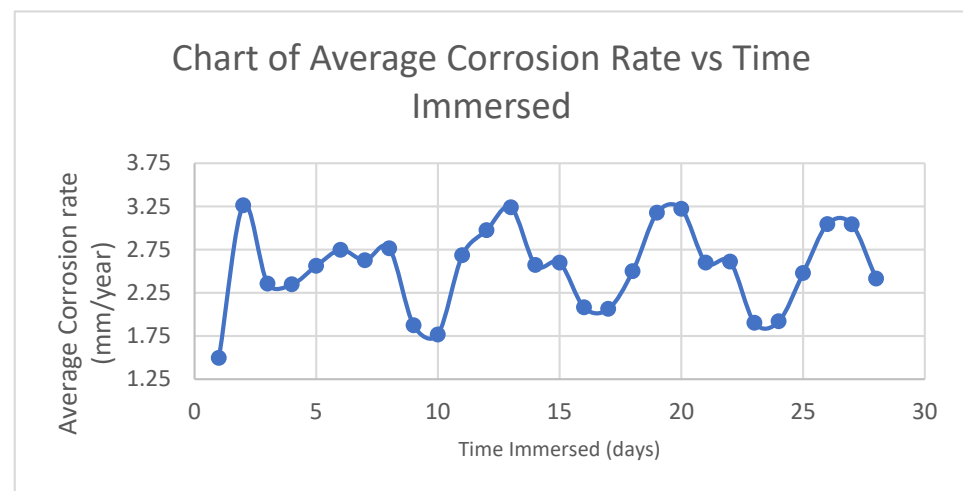


Figure 10. Chart of average corrosion rate vs. time immersed for Mg-5Se-2Zn-2SiO₂ composite.

Over the 28 days, the average weight loss was approximately 2.6 mm/year and was compared with pure Mg in Table 9. After 28 days of immersion, the sample retained structural integrity.

Table 9. Average corrosion rate of Mg-5Se-2Zn-2SiO₂, with pure Mg as a reference.

Material	Average Corrosion Rate (mm/year)
Pure Mg, extruded [22,23]	1.2
Pure Mg, extruded and cold drawn [22,24]	1.6–2.2
Mg-5Se-2Zn-2SiO ₂	2.6 ± 0.5

3.7. Thermal Characterization

Figure 11 shows the trend of temperature with elapsed time for the magnesium matrix composite. This plot was used to ascertain the ignition temperature, which is the temperature just before the small peak observed. The ignition temperature is recorded below in Table 10. The ignition temperature of the Mg-5Se-2Zn-2SiO₂ was 30 °C higher (an increase of 5%).

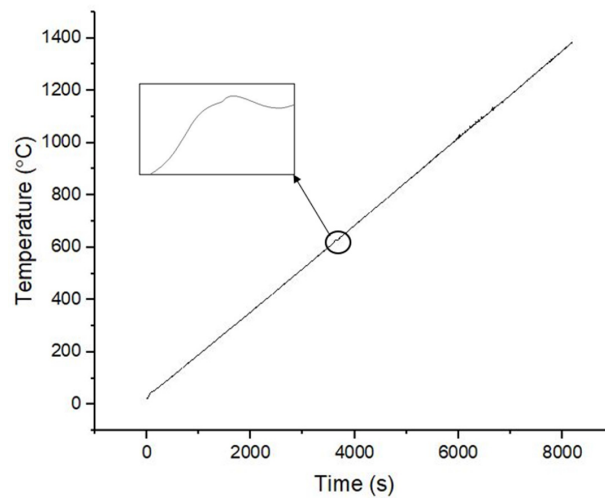


Figure 11. TGA results of Mg-5Se-2Zn-2SiO₂.

Table 10. Ignition temperature of Mg-5Se-2Zn-2SiO₂ and pure magnesium as a reference.

Material	Ignition Temperature (°C)
Pure Mg * [21]	590
Mg-5Se-2Zn-2SiO ₂	620 (↑5%)

* Material has been synthesized using similar method (DMD followed by hot extrusion).

Figure 12 shows the trend of heat flow with temperature for the magnesium matrix composite. A small exothermic peak is observed at 564 °C.

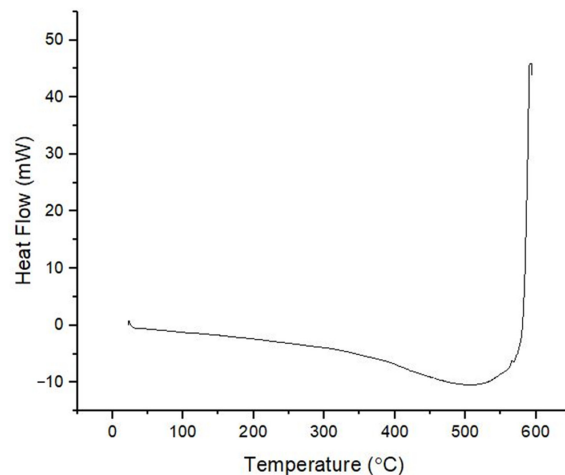


Figure 12. DSC results of Mg-5Se-2Zn-2SiO₂.

Table 11 shows the coefficient of thermal expansion for Mg-5Se-2Zn-2SiO₂ and pure magnesium. Mg-5Se-2Zn-2SiO₂ exhibited a 6% lower CTE, indicating its higher thermal stability.

Table 11. Coefficient of thermal expansion for Mg-5Se-2Zn-2SiO₂ and pure magnesium as a reference.

Material	Average Coefficient of Thermal Expansion ($\times 10^{-6}$ K)
Pure Mg [25]	26.00
Mg-5Se-2Zn-2SiO ₂	24.57 \pm 2.25 (\downarrow 6%)

4. Discussion

4.1. Synthesis

The resulting loss of selenium within the material underscores a need for loss-prevention measures when using selenium (with a melting point of 220.8 °C and boiling point of 685 °C [26]) as an alloying element in the synthesis of materials involving elevated temperatures, especially those exceeding its boiling point, as was performed with DMD processing with a target superheat temperature of 750 °C in this study.

It was also demonstrated that the hot extrusion of selenium-containing magnesium materials can be conducted at temperatures beyond that of selenium's melting point. These observations underscore the importance of process parameter optimization.

4.2. Microstructure

Based on the SEM and EDS results, it can be observed that the elements in the Mg-5Se-2Zn-2SiO₂ material were well distributed. The zinc and silicon dioxide are well dispersed in the background and there are swirls of selenium in Mg-deficient regions, as shown by the mapping results. These can be explained due to the low solubility of selenium in magnesium [27]. The presence of MgO could be attributed to the oxidation of magnesium, either during synthesis or during sample preparation, where it is difficult to eliminate oxides entirely. The regions with a high Se content can also be attributed to the formation of MgSe, supported by DSC results, as further elaborated in Section 4.7.

As magnesium comprised the vast majority of the material, most dominant peaks corresponded to it. Peaks corresponding to intermetallic phases of Mg₂Si and MgSe were detected. The Mg₂Si peak had a relatively low intensity, which could be indicative of the limited reaction between Mg and SiO₂ nanoparticles.

The decrease in the grain size resulted in an increase in strength and hardness as per the Hall–Petch relationship, since the grain size is within the micron range [28]. This can be attributed to presence of selenium as a grain refiner [29], as well as the presence of MgSe, Mg₂Si, MgO and nano-sized SiO₂ within the Mg matrix, as previously observed by Parande et al. [30].

4.3. Density and Porosity

The average experimental and theoretical density for Mg-5Se-2Zn-2SiO₂ is higher than that of pure magnesium. This could be attributed to the addition of elements such as zinc (7.14 g/cm³), silicon dioxide (2.4 g/cm³) and selenium (4.28 g/cm³), which all have a higher density when compared to magnesium.

The elemental analysis results revealed significant selenium loss (less than 1 wt.% was detected against the 5 wt.% initially used in the synthesis). As mentioned in Section 4.1, this was likely due to the evaporation of selenium during the DMD process.

The experimental density of Mg-5Se-2Zn-2SiO₂ is higher than the theoretical density, this could possibly be due to formation of MgO and SeO₂, considering their high affinity with oxygen [31]. The formation of these oxides can, in turn, cause the experimental density to be higher than the theoretical density. The true porosity value, calculated by the pore area fraction, was less than 1%, which is consistent with other Mg composites synthesized using DMD [32].

4.4. Damping Characterization

The damping properties were found to be substantially enhanced for the MMC when compared to pure magnesium. This is correlated with the SiO₂ addition to pure Mg, where the resulting damping loss rate, representing the material's ability to absorb or stop vibrations, was significantly enhanced [30,33]. Silicon dioxide has potential as a vibration-absorbent material [34] because of its visco-elastic properties, which results in higher energy dissipation as heat, hence leading to superior damping capabilities [35].

The elastic modulus of Mg-5Se-2Zn-2SiO₂ was quite similar (3% increase) to that of pure magnesium. Considering the Young's modulus of human cortical bone (ranging from 12.6 to 27 GPa [36–38]) magnesium-based materials such as the current one provide the best option to mitigate stress shielding when compared to steels and titanium and Co-based alloys.

4.5. Mechanical Characterization

An increase in microhardness was observed for the Mg-5Se-2Zn-2SiO₂ matrix composite. This could be attributed to the refinement in grain size [39]. As per the Hall–Petch relationship, smaller grain sizes can impede dislocation, which increases hardness by hindering plastic deformation. Additionally, silicon dioxide nanoparticles can act as barriers to dislocation by strengthening the grain boundaries [40]; this in turn also restricts dislocation motion and plastic deformation, thereby increasing the hardness. Lastly, the presence of silicon dioxide and magnesium silicide (Mg₂Si) can increase overall hardness because of their hardnesses of 7.3 GPa [41] and 4.5 GPa [42], respectively, which is significantly greater than that of magnesium.

The Mg-5Se-2Zn-2SiO₂ matrix composite exhibited higher yield strength (157% increase), ultimate compressive strength (54% increase), and fracture strain (39% increase) values when compared to pure magnesium, owing to the well-known Hall–Petch effect arising [43] from grain size refinement h . This is because grain boundaries can act as an obstruction to dislocation via pile-ups [44,45], which in turn increases the yield strength and ultimate compressive strength. Additionally, silicon dioxide has compressive strength ranging between 1100 and 1380 MPa [46], which is also higher than magnesium's. Therefore, the use of silicon dioxide as high-strength ceramic nanosized reinforcement is effective in enhancing the compressive properties of Mg-based matrix composites.

Furthermore, the Mg-5Se-2Zn-2SiO₂ MMC exhibited a significant increase in fracture strain, indicating that the MMC has a higher ductility. One of the major drawbacks of using magnesium materials is their relatively poor ductility [2,47] compared to other metallic biomaterials, such as including titanium and stainless steel [48]. The improved ductility of a Mg-5Se-2Zn-2SiO₂ composite allows easier fabrication and contouring for intricate shapes, which can be leveraged for purpose-built structural and biomedical designs.

Shear bands were observed on the fracture surface. The compressive failure occurred as a result of the shear mode for the composite. However, a few cracks were observed near the edge of the surface, which could result from the high fracture strain value for the composite when compared to pure magnesium.

4.6. Corrosion Testing

Mg-5Se-2Zn-2SiO₂ was found to have acceptable corrosion resistance when compared to pure magnesium. This could be attributed to the addition of silicon dioxide (bioceramic) nanoparticles to the composite, which forms a precipitate film on the surface [49]. This reduces the contact of the composite with the solution, thereby reducing the corrosion rate. The addition of selenium and zinc to metal alloys or composites can result in increased corrosion rates as intermetallic phases can act as micro-sized galvanic cells [49]. Selenium also has a Pilling–Bedworth Ratio (PBR) of 1.69 [50], which indicates its ability to form a protective oxide layer and inhibit further corrosion.

The presence of nano-scale SiO₂ as reinforcement also possibly impacted the corrosion rate; previous work with AZ31 alloy with Al₂O₃ nanocomposites showed a formation of

a thin but compact oxide layer on the surface [51]. With regard to corrosion resistance, a reduction in the amount of cathodic phases within the matrix would lead to reduction in number of galvanic cells and a decrease in grain size would also lead to a more coherent oxide surface [52], leading to overall lower corrosion rates.

4.7. Thermal Characterization

Mg-5Se-2Zn-2SiO₂ had a slightly higher ignition temperature than that of pure magnesium. This could be due to the addition of SiO₂ nanoparticles, which are thermally stable up to 1300 °C [53] due to the presence of strong covalent bonds, underscoring the ability of ceramics to increase the ignition resistance of Mg-materials.

The small exothermic peak observed at 564 °C can be attributed to a reaction between Mg and selenium dioxide, to give magnesium selenide in an inert environment [54]. The thermodynamics of this reaction were studied by Mills [55,56], who estimated its enthalpy of formation to be −293 kJ/mol, indicating its exothermic nature. This is further supported by the detection of a MgSe peak in XRD analysis as shown earlier, indicating its presence.

The Mg-5Se-2Zn-2SiO₂ matrix composite was observed to have a lower CTE value than pure magnesium, thus having an improved dimensional stability. This is because the CTE value of silicon dioxide (0.24×10^{-6} K) [57] is much lower than that of pure magnesium (26×10^{-6} K). This CTE mismatch contributes to the reduction in CTE for the overall metal matrix composite [58].

5. Conclusions

The synthesis of a Mg-5Se-2Zn-2SiO₂ matrix composite via DMD and extrusion was successful. Based on the characterization conducted, the following conclusions can be drawn from this study:

1. Selenium loss in synthesis needs to be addressed with loss-prevention measures.
2. Mg-5Se-2Zn-2SiO₂ experienced significant grain refinement (80% reduction in size) and an increased hardness of 32% when compared to pure magnesium.
3. Mg-5Se-2Zn-2SiO₂ had a similar Young's modulus to that of pure magnesium, with only a difference of 3%, whilst having a significantly higher attenuation coefficient, (178% increase) and a lower true porosity of about 31%.
4. For compressive properties, the 0.2% yield strength (157% higher), ultimate yield strength (54% higher), fracture strain (39% higher), and energy absorbed (112% higher) were all higher for Mg-5Se-2Zn-2SiO₂, demonstrating its superiority over pure Mg in this context.
5. Mg-5Se-2Zn-2SiO₂ had a slightly higher ignition temperature (5% lower) and 6% lower coefficient of thermal expansion when compared to pure magnesium.
6. Mg-5Se-2Zn-2SiO₂ had a higher, but still acceptable, corrosion rate when compared to pure magnesium. The sample maintained structural integrity even after 28 days in PBS solution.

Considering the promising properties exhibited by this material in conjunction with the use of biocompatible additions, further studies involving not just optimized synthesis parameters/loss prevention measures but also alternative synthesis methods (e.g., Powder Metallurgy or Turning-Induced Deformation) are viable options. Furthermore, post-treatment of samples (such as heat or cryogenic treatment) can also lead to potential property enhancements, which increases domain knowledge and their potential for use in the biomedical field.

Author Contributions: Conceptualization, M.G.; methodology, M.J. and M.G.; validation, M.J.; formal analysis, M.J. and A.P.; investigation, A.P.; resources, M.J. and M.G.; data curation, M.J. and A.P.; writing—original draft preparation, A.P.; writing—review and editing, M.J. and M.G.; visualization, M.J. and A.P.; supervision, M.G.; project administration, M.J. and M.G. All authors have read and agreed to the published version of the manuscript.

Funding: This research received no external funding.

Data Availability Statement: The data presented in this study are available on request from the corresponding author. The data are not publicly available due to confidentiality of research in some aspects.

Acknowledgments: The authors acknowledge Juraimi Bin Madon for assistance with extrusion and Ng Hong Wei for assistance with TGA, DSC, and CTE testing.

Conflicts of Interest: The authors declare no conflicts of interest.

References

- Al-Shalawi, F.D.; Mohamed Ariff, A.H.; Jung, D.W.; Mohd Ariffin, M.K.A.; Seng Kim, C.L.; Brabazon, D.; Al-Osaimi, M.O. Biomaterials as Implants in the Orthopedic Field for Regenerative Medicine: Metal versus Synthetic Polymers. *Polymers* **2023**, *15*, 2601. [CrossRef] [PubMed]
- Sezer, N.; Evis, Z.; Murat Kayhan, S.; Tahmasebifar, A.; Koç, M. Review of magnesium-based biomaterials and their applications. *J. Magnes. Alloys* **2018**, *6*, 23–43. [CrossRef]
- Herber, V.; Okutan, B.; Antonoglou, G.; Sommer, N.G.; Payer, M. Bioresorbable Magnesium-Based Alloys as Novel Biomaterials in Oral Bone Regeneration: General Review and Clinical Perspectives. *J. Clin. Med.* **2021**, *10*, 1842. [CrossRef] [PubMed]
- Pogorielov, M.; Husak, E.; Solodivnik, A.; Zhdanov, S. Magnesium-based biodegradable alloys: Degradation, application, and alloying elements. *Interv. Med. Appl. Sci.* **2017**, *9*, 27–38. [CrossRef]
- Kyu Cho, T.S.; Doherty, K.; Yen, C.; Gazonas, G.; Montgomery, J.; Moy, P. Magnesium Technology and Manufacturing for Ultra Lightweight Armored Ground Vehicle. In Proceedings of the 2008 Army Science Conference, Orlando, FL, USA, 3 December 2008.
- Moghadas, K.; Mohd Isa, M.S.; Ariffin, M.A.; Mohd Jamil, M.Z.; Raja, S.; Wu, B.; Yamani, M.; Bin Muhamad, M.R.; Yusof, F.; Jamaludin, M.F.; et al. A review on biomedical implant materials and the effect of friction stir based techniques on their mechanical and tribological properties. *J. Mater. Res. Technol.* **2022**, *17*, 1054–1121. [CrossRef]
- Zhang, S.; Zhang, X.; Zhao, C.; Li, J.; Song, Y.; Xie, C.; Tao, H.; Zhang, Y.; He, Y.; Jiang, Y.; et al. Research on an Mg-Zn alloy as a degradable biomaterial. *Acta Biomater.* **2010**, *6*, 626–640. [CrossRef]
- Huang, X.; Dong, Z.; Liu, J.; Mao, S.; Xu, J.; Luo, G.; Shen, J. Selenium-Mediated Micellar Catalyst: An Efficient Enzyme Model for Glutathione Peroxidase-like Catalysis. *Langmuir* **2007**, *23*, 1518–1522. [CrossRef] [PubMed]
- Huang, Y.; Su, E.; Ren, J.; Qu, X. The recent biological applications of selenium-based nanomaterials. *Nano Today* **2021**, *38*, 101205. [CrossRef]
- Huang, Y.; Li, P.; Zhao, R.; Zhao, L.; Liu, J.; Peng, S.; Fu, X.; Wang, X.; Luo, R.; Wang, R.; et al. Silica nanoparticles: Biomedical applications and toxicity. *Biomed. Pharmacother.* **2022**, *151*, 113053. [CrossRef]
- Kuršvietienė, L.; Mongirdienė, A.; Bernatoniene, J.; Šulinskiene, J.; Stanevičienė, I. Selenium Anticancer Properties and Impact on Cellular Redox Status. *Antioxidants* **2020**, *9*, 80. [CrossRef]
- Zhang, Q.; Qian, Z.-Y.; Zhou, P.-H.; Zhou, X.-l.; Zhang, D.-L.; He, N.; Zhang, J.; Liu, Y.-H.; Gu, Q. Effects of oral selenium and magnesium co-supplementation on lipid metabolism, antioxidative status, histopathological lesions, and related gene expression in rats fed a high-fat diet. *Lipids Health Dis.* **2018**, *17*, 165. [CrossRef]
- Wan, Y.; Cui, T.; Li, W.; Li, C.; Xiao, J.; Zhu, Y.; Ji, D.; Xiong, G.; Luo, H. Mechanical and biological properties of bio-glass/magnesium composites prepared via microwave sintering route. *Mater. Des.* **2016**, *99*, 521–527. [CrossRef]
- Nie, K.B.; Wang, X.J.; Deng, K.K.; Hu, X.S.; Wu, K. Magnesium matrix composite reinforced by nanoparticles—A review. *J. Magnes. Alloys* **2021**, *9*, 57–77. [CrossRef]
- Wang, X.J.; Hu, X.S.; Wang, Y.Q.; Nie, K.B.; Wu, K.; Zheng, M.Y. Microstructure evolutions of SiCp/AZ91 Mg matrix composites during hot compression. *Mater. Sci. Eng. A* **2013**, *559*, 139–146. [CrossRef]
- Gupta, M.; Wong, W.L.E. High Performance Magnesium Based Composites Containing Nano-Length Scale/Amorphous/Hollow Reinforcements. *Mater. Sci. Forum* **2016**, *879*, 642–647. [CrossRef]
- Tun, K.S.; Nahata, A.; Vincent, S.; Gupta, M. Development of a Low Entropy, Lightweight, Multicomponent, High Performance (Hardness + Strength + Ductility) Magnesium-Based Alloy. *JOM* **2023**, *75*, 459–469. [CrossRef]
- Johanes, M.; Tekumalla, S.; Gupta, M. Fe₃O₄ Nanoparticle-Reinforced Magnesium Nanocomposites Processed via Disintegrated Melt Deposition and Turning-Induced Deformation Techniques. *Metals* **2019**, *9*, 1225. [CrossRef]
- Office of Dietary Supplements. Selenium. Available online: <https://ods.od.nih.gov/factsheets/Selenium-HealthProfessional/> (accessed on 4 January 2024).
- Gates-Rector, S.; Blanton, T. The Powder Diffraction File: A quality materials characterization database. *Powder Diffr.* **2019**, *34*, 352–360. [CrossRef]
- Tekumalla, S.; Yang, C.; Seetharaman, S.; Wong, W.L.E.; Goh, C.S.; Shabadi, R.; Gupta, M. Enhancing overall static/dynamic/damping/ignition response of magnesium through the addition of lower amounts (<2%) of yttrium. *J. Alloys Compd.* **2016**, *689*, 350–358.
- Atrens, A.; Shi, Z.; Mehreen, S.U.; Johnston, S.; Song, G.-L.; Chen, X.; Pan, F. Review of Mg alloy corrosion rates. *J. Magnes. Alloys* **2020**, *8*, 989–998. [CrossRef]
- Dvorský, D.; Kubásek, J.; Voňavková, I.; Vojtěch, D. Structure, mechanical and corrosion properties of extruded Mg-Nd-Zn, Mg-Y-Zn and Mg-Y-Nd alloys. *Mater. Sci. Technol.* **2019**, *35*, 520–529. [CrossRef]

24. Zuo, M.; Wang, W.; Wu, H.; Yang, L.; Yan, J.; Ni, J.; Zhang, S.; Song, Y.; Wang, J.; Zhang, X. In vitro degradation and mineralization of high-purity magnesium in three physiological fluids. *Mater. Lett.* **2019**, *240*, 279–283. [CrossRef]
25. Wang, C.; Dong, Z.; Jiang, B.; Zheng, Z.; Wu, S.; Song, J.; Zhang, A.; Xu, J.; Yang, B.; Zheng, C.; et al. Lowering thermal expansion of Mg with the enhanced strength by Ca alloying. *J. Mater. Res. Technol.* **2023**, *24*, 1293–1303. [CrossRef]
26. Royal Society of Chemistry. Selenium. Available online: <https://www.rsc.org/periodic-table/element/34/selenium> (accessed on 26 December 2023).
27. Rashad, M.; Zaidi, S.D.A.; Asif, M. Debating the magnesium–selenium battery technology. *J. Magnes. Alloys* **2020**, *8*, 980–988. [CrossRef]
28. Hannink, R.H.J.; Hill, A.J. 9—Nanoengineering of metallic materials. In *Nanostructure Control of Materials*; Woodhead Publishing: Cambridge, UK, 2006.
29. Pavlov, D.; Dimitrov, M.; Petkova, G.; Giess, H.; Gnehm, C. The Effect of Selenium on the Electrochemical Behavior and Corrosion of Pb-Sn Alloys Used in Lead-Acid Batteries. *J. Electrochem. Soc.* **1995**, *142*, 2919–2927. [CrossRef]
30. Parande, G.; Manakari, V.; Meenashisundaram, G.K.; Gupta, M. Enhancing the hardness/compression/damping response of magnesium by reinforcing with biocompatible silica nanoparticulates. *Int. J. Mater. Res.* **2016**, *107*, 1091–1099. [CrossRef]
31. Tan, Q.; Atrens, A.; Mo, N.; Zhang, M.-X. Oxidation of magnesium alloys at elevated temperatures in air: A review. *Corros. Sci.* **2016**, *112*, 734–759. [CrossRef]
32. Penchal Reddy, M.; Manakari, V.; Parande, G.; Ubaid, F.; Shakoor, R.A.; Mohamed, A.M.A.; Gupta, M. Enhancing compressive, tensile, thermal and damping response of pure Al using BN nanoparticles. *J. Alloys Compd.* **2018**, *762*, 398–408. [CrossRef]
33. Nguyen, Q.B.; Nai, M.L.S.; Nguyen, A.S.; Seetharaman, S.; Jayalakshmi, S.; Leong, E.W.W.; Gupta, M. Microstructure and damping characteristics of Mg and its composites containing metastable Al₈₅Ti₁₅ particle. *J. Compos. Mater.* **2015**, *50*, 2565–2573. [CrossRef]
34. Asadi Khanouki, M.; Ohadi, A.R. Improved acoustic damping in polyurethane foams by the inclusion of silicon dioxide nanoparticles. *Adv. Polym. Technol.* **2018**, *37*, 2799–2810. [CrossRef]
35. Shamim Hasan, A.H.M.; Chowdbury, M.A.; Almahri, A.; Kowser, M.A.; Alam, M.S.; Ahmed Shuvho, M.B.; Alruwais, R.S.; Hossain, N.; Rahman, M.R.; Rahman, M.M. Physical, thermal, and mechanical properties of Al₂O₃/SiO₂ infused jute/glass fiber resin composite materials in relation to viscosity. *Polym. Compos.* **2022**, *43*, 3971–3982. [CrossRef]
36. Rho, J.Y.; Ashman, R.B.; Turner, C.H. Young’s modulus of trabecular and cortical bone material: Ultrasonic and microtensile measurements. *J. Biomech.* **1993**, *26*, 111–119. [CrossRef]
37. Mirzaali, M.J.; Schwiedrzik, J.J.; Thaiwichai, S.; Best, J.P.; Michler, J.; Zysset, P.K.; Wolfram, U. Mechanical properties of cortical bone and their relationships with age, gender, composition and microindentation properties in the elderly. *Bone* **2016**, *93*, 196–211. [CrossRef]
38. Rho, J.-Y.; Tsui, T.Y.; Pharr, G.M. Elastic properties of human cortical and trabecular lamellar bone measured by nanoindentation. *Biomaterials* **1997**, *18*, 1325–1330. [CrossRef]
39. Parande, G.; Manakari, V.; Prasad, S.; Chauhan, D.; Rahate, S.; Wong, R.; Gupta, M. Strength retention, corrosion control and biocompatibility of Mg-Zn-Si/HA nanocomposites. *J. Mech. Behav. Biomed. Mater.* **2020**, *103*, 103584. [CrossRef]
40. Moustafa, E.B.; Taha, M.A. The Effect of Mono and Hybrid Additives of Ceramic Nanoparticles on the Tribological Behavior and Mechanical Characteristics of an Al-Based Composite Matrix Produced by Friction Stir Processing. *Nanomaterials* **2023**, *13*, 2148. [CrossRef]
41. Michel, M.D.; Serbena, F.C.; Lepienski, C.M. Effect of temperature on hardness and indentation cracking of fused silica. *J. Non-Cryst. Solids* **2006**, *352*, 3550–3555. [CrossRef]
42. Lu, L.; Lai, M.O.; Hoe, M.L. Formation of Nanocrystalline Mg₂Si AND Mg₂Si Dispersion Strengthened Mg-Al Alloy by Mechanical Alloying. *Nanostructured Mater.* **1998**, *10*, 551–563. [CrossRef]
43. Yu, H.; Xin, Y.; Wang, M.; Liu, Q. Hall-Petch relationship in Mg alloys: A review. *J. Mater. Sci. Technol.* **2018**, *34*, 248–256. [CrossRef]
44. Hall, E.O. The Deformation and Ageing of Mild Steel: III Discussion of Results. *Proc. Phys. Soc. Sect. B* **1951**, *64*, 747. [CrossRef]
45. Petch, N. The orientation relationships between cementite and α -iron. *Acta Crystallogr.* **1953**, *6*, 96. [CrossRef]
46. Lines, M. Silica—Silicon Dioxide (SiO₂). Available online: <https://www.azom.com/article.aspx?ArticleID=1114> (accessed on 11 June 2023).
47. Zhang, T.; Wang, W.; Liu, J.; Wang, L.; Tang, Y.; Wang, K. A review on magnesium alloys for biomedical applications. *Front. Bioeng. Biotechnol.* **2022**, *10*, 953344. [CrossRef]
48. Wu, S.; Liu, X.; Yeung, K.W.K.; Guo, H.; Li, P.; Hu, T.; Chung, C.Y.; Chu, P.K. Surface nano-architectures and their effects on the mechanical properties and corrosion behavior of Ti-based orthopedic implants. *Surf. Coat. Technol.* **2013**, *233*, 13–26. [CrossRef]
49. Delavar, H.; Mostahsan, A.J.; Ibrahim, H. Corrosion and corrosion-fatigue behavior of magnesium metal matrix composites for bio-implant applications: A review. *J. Magnes. Alloys* **2023**, *11*, 1125–1161. [CrossRef]
50. Syvertsen, M. Oxide Skin Strength on Molten AA5XXX Aluminum Alloy—Effect of Beryllium and Alternatives. In *Light Metals 2017*; Springer: Cham, Switzerland, 2017; pp. 1451–1455.
51. Nguyen, Q.B.; Gupta, M.; Srivatsan, T.S. On the role of nano-alumina particulate reinforcements in enhancing the oxidation resistance of magnesium alloy AZ31B. *Mater. Sci. Eng. A* **2009**, *500*, 233–237. [CrossRef]

52. Kukreja, M.; Balasubramaniam, R.; Nguyen, Q.B.; Gupta, M. Enhancing corrosion resistance of Mg alloy AZ31B in NaCl solution using alumina reinforcement at nanolength scale. *Corros. Eng. Sci. Technol.* **2009**, *44*, 381–383. [[CrossRef](#)]
53. Liehr, M.; Lewis, J.E.; Rubloff, G.W. Kinetics of high-temperature thermal decomposition of SiO₂ on Si(100). *J. Vac. Sci. Technol. A Vac. Surf. Films* **1987**, *5*, 1559–1562. [[CrossRef](#)]
54. ChemicalBook Inc. Magnesium Selenide. Available online: https://www.chemicalbook.com/ChemicalProductProperty_EN_CB6937531.htm (accessed on 26 December 2023).
55. Mills, K.C. *Thermodynamic Data for Inorganic Sulphides, Selenides and Tellurides*; Butterworths: London, UK, 1974.
56. Olin, Å.; Noläng, B.I.; Öhman, L.; Osadchii, E.G.; Rosén, E. *Chemical Thermodynamics of Selenium*; Elsevier: Amsterdam, The Netherlands, 2005.
57. Tsou, C.; Huang, Y.-S.; Li, H.-C.; Lai, T.-H. Determination of Thermal Expansion Coefficient of Thermal Oxide. *Sens. Mater.* **2005**, *17*, 441–451.
58. Sheng, J.; Wang, L.; Li, S.; Yin, B.; Liu, X.; Fei, W.-D. Phase-Transformation-Induced Extra Thermal Expansion Behavior of (Sr_xBa_{1-x})TiO₃/Cu Composite. *Sci. Rep.* **2016**, *6*, 27118. [[CrossRef](#)]

Disclaimer/Publisher's Note: The statements, opinions and data contained in all publications are solely those of the individual author(s) and contributor(s) and not of MDPI and/or the editor(s). MDPI and/or the editor(s) disclaim responsibility for any injury to people or property resulting from any ideas, methods, instructions or products referred to in the content.